Research Article
Vol. 29, No. 20 / 27 Sep 2021 / Optics Express 31465
Optics EXPRESS

Tin reduction from fluorine doped tin oxide for silicon nanowire-based solar energy harvesting and storage

HALAGACKA LUKAS,[1,2,3,6] GELNAROVA ZUZANA,[2,3] AL-GHZAIWAT MUTAZ,[1,4] FLOREA ILEANA,[1] HORNICEK JIRI,[3] POSTAVA KAMIL,[2,3,5] AND FOLDYNA MARTIN[1,7]

[1] *LPICM, CNRS, Ecole Polytechnique, Institut Polytechnique de Paris, 91128 Palaiseau, France*
[2] *IT4Innovation, VŠB - Technical University of Ostrava, 17 listopadu 15, 708 00 Ostrava-Poruba, Czech Republic*
[3] *Nanotechnology Centre, CEET, VŠB - Technical University of Ostrava, 17 listopadu 15, 708 00 Ostrava-Poruba, Czech Republic*
[4] *Department of Renewable Energy Engineering, Middle East University, 11831 Amman, Jordan*
[5] *Faculty of Materials Science and Technology, VŠB - Technical University of Ostrava, 17 listopadu 15, 708 00 Ostrava-Poruba, Czech Republic*
[6] *lukas.halagacka@vsb.cz*
[7] *martin.foldyna@polytechnique.edu*

Abstract: Hydrogen plasma reduction of fluorine doped tin oxide is a beneficial method to form tin nanodroplets on the sample surface directly in the plasma-enhanced chemical vapor deposition reactor. The formation of catalyst droplets is a crucial initial step for vapor-liquid-solid growth of silicon nanowires for radial junction solar cells and solar fuel cell technology. We present an original optical model which allows us to trace the formation process on fluorine doped tin oxide on soda-lime glass substrate from the in situ data and is in a good agreement with the spectroscopic ellipsometry data measured before and during the reduction process. The model reproduces well the phase shift introduced by a transition double layer in fluorine doped tin oxide which acts as a barrier against the sodium diffusion. Furthermore, we study the process of tin reduction from fluorine doped tin oxide in a real time and compare estimated amount of produced metallic tin with images from scanning electron microscopy.The proposed approach is very important for in situ real-time monitoring of the one-pump-down fabrication process used to grow nanowires and form radial junction devices.

© 2021 Optical Society of America under the terms of the OSA Open Access Publishing Agreement

1. Introduction

Tin nanodroplets which catalyze silicon nanowire (SiNW) growth can be formed from thermally evaporated tin film on substrate. Misra et al. [1] achieved 9.2% efficiency on radial junction solar cell built on silicon nanowires grown on a glass substrate using thermally evaporated 1 – 5 nm thick Sn layer. However, this approach require extra process step of Sn thermal evaporation. Their method can be further improved to one-pump-down process when direct tin reduction from fluorine doped tin oxide (FTO) commercial substrates in plasma-enhanced chemical vapor deposition (PECVD) reactor instead of thermal evaporation is employed [2]. This approach is well-compatible with industrial fabrication processes and lowers a risk of sample contamination. FTO layer acts as the source of Sn catalyst as well as the back electrode in this case. Since FTO is a well-established transparent conductive oxide, it can be conveniently used for albedo collecting bifacial solar cells.

#435500
Journal © 2021
https://doi.org/10.1364/OE.435500
Received 30 Jun 2021; revised 20 Aug 2021; accepted 20 Aug 2021; published 16 Sep 2021

In situ spectroscopic ellipsometry (SE) is a convenient technique which enables real-time, non-destructive, and non-invasive characterization of the fabrication process directly in a plasma-enhanced chemical vapor deposition reactor. In a previous in situ SE study of the SiNWs growth it was demonstrated how the optical model can be built up to describe the growth process [3]. However, to be able to perform an in situ study of the growth on different substrates, the knowledge of substrate's optical functions is essential. In Ref. [4] a-Si:H/SnO_2:F textured structures on glass substrate are studied and the optical functions of FTO are introduced. However, the FTO optical functions are presented only in a limited spectral range up to 3 eV, which is insufficient for purposes of our target applications and wider spectral range. In addition, published FTO material (see [4]) shows interband optical absorptions starting already from 2 eV. In constrast, FTO material in our study shows transparency up to 4.5 eV which is suitable for high efficiency solar energy harvesting applications. Therefore, the new wide spectral range optical model of FTO is needed.

In this paper, we monitor the hydrogen plasma reduction of tin from FTO in real time using in situ spectroscopic ellipsometry. The reduction duration strongly determines the final morphology of the surface [5]. In the first part of the paper we present original model of the FTO layer on a soda-lime glass substrate. Such a structure is typically frequently used and commercially available for perspective silicon nanowire-based photovoltaic devices, but its complete model has not been reported so far. The developed model is simple (low number of fitting parameters) and it enables to describe different substrates provided by various commercial suppliers. At the same time, the model is robust-enough to fit in situ SE data which are commonly affected by problems related to installation of an ellipsometer on a reactor (i.e. fixed angle of incidence, effect of windows located on vacuum chamber, alignment of the system). In the second part, we show how this optical model can be further extended to trace the amount of reduced tin in the real time and hence to better control the fabrication process.

2. Studied samples and experimental methods

2.1. Sample of fluorine doped tin oxide on glass substrate

In this study we have used 25×25 mm^2 commercial substrates with 600 nm nominal thick layer of FTO on a 2.2 mm thick standard substrate of a soda-lime glass (SLG). The FTO layer was deposited by chemical vapor deposition (CVD) technique. Figure 1(a) shows a transmission electron microscopy (TEM) cross-sectional image of the studied sample. TEM analysis were performed on a new generation Titan Themis transmission electron microscope operated at 300 kV. An additional transition double layer between glass substrate and the FTO layer is clearly visible. In addition, the figure shows the profile of the surface roughness of the FTO layer. Figure 1(b) shows detail of the transition double layer consisting of crystalline phase on the glass covered with an amorphous material and followed by the FTO layer. These TEM observations of the transition double layer and surface roughness are crucial for a development of the optical model of the studied FTO sample.

2.2. Hydrogen plasma reduction of tin from FTO

Tin catalyst nanoparticles were formed from the FTO by a direct hydrogen plasma reduction in the PECVD reactor. At first, studied sample was loaded to a capacitively coupled radio frequency (13.56 MHz) PECVD reactor. After reaching base pressure of 5×10^{-6} mbar, the temperature was increased to 200 °C. Hydrogen plasma was ignited after introduction of 100 standard cubic centimeters per minute (sccm) of hydrogen at the pressure of 0.8 mbar with the RF power of 5 W and with the inner distance between electrodes fixed to 28 mm [2].

Optics EXPRESS

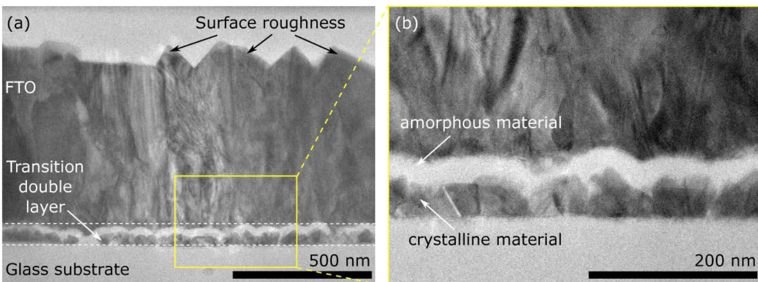

Fig. 1. TEM images observed on cross-sectional slice of studied FTO layer on glass substrate. (a) Section of the sample showing full view on the FTO layer with top surface roughness and bottom transition double layer. (b) Detail on the bottom double layer showing part of small crystals on the glass followed by amorphous material.

2.3. Ex situ and in situ spectroscopic ellipsometry

In our study, two spectroscopic ellipsometers were used. The Woollam RC2–DI for ex-situ and Woollam M–2000DI mounted on the reactor chamber for in situ measurements, respectively. Although both spectroscopic ellipsometers have the same spectral range 0.73 eV - 6.42 eV, the data are only collected from 1 eV to 6.42 eV (193 nm - 1240 nm) owing to a low signal intensity in the infrared range below 1 eV. The ex-situ ellipsometer with two continuously rotating compensators was used for variable angle of incidence measurements and integration time was 20 s. The angle of incidence of the in situ ellipsometer was 72.1° (obtained during the system calibration), the integration time was 3 s and the repetition rate 10 s. The one zone measurement with azimuthal angle of 45° for polarizer and rotating compensator was used.

Optical response of the system without s- to p-polarization mode conversion and depolarizations is described by the ellipsometric angles ψ and Δ, which are directly related to the measured ellipsometric quantities N, C, and S [6]:

$$N = \cos 2\psi, \quad C = \sin 2\psi \cos \Delta, \quad S = \sin 2\psi \sin \Delta. \tag{1}$$

To compare with experimental SE data the optical multi-layered model of the measured sample has to be developed and parameterized. In the SE data analysis, the Levenberg-Marquardt least-square minimization algorithm [7] was used. The following merit function χ^2 was used as a criterion for the model to data fit of a single spectrum:

$$\chi^2 = \frac{1}{3K - L - 1} \left[\sum_{k=1}^{K} \frac{\sum_{X \in \{N,C,S\}} \left(X_k^{meas.} - X_k^{mod.} \right)^2}{\sigma_k^2} \right], \tag{2}$$

where N, C, and S are ellipsometric quantities defined by Eq. (1). Superscripts *meas.* and *mod.* stand for measured and modeled data, respectively. Value of the estimated measurement error $\sigma_k = 0.001$ was used for all models and spectral points to acquire comparable values of merit function. K is the number of spectral points (1088 and 710 for ex-situ and in situ data, respectively), and L is the number of fitted parameters.

3. Results and discussions

The presented optical study of the Sn reduction from FTO by the hydrogen plasma in a PECVD reactor is divided into two main parts. In the first part the optical model based on a multi-layered model and parametric complex dielectric function ($\epsilon = \epsilon_1 + i\epsilon_2$) of FTO layer on SLG substrate is

Optics EXPRESS

developed. The model is validated by a multi-angle SE data fitting. In addition, optical functions of metallic Sn are determined from a reference sample, since these will be needed to model the metallic tin reduction from FTO in the next step. In the second part developed models of FTO and Sn are used for analysis of the SE data measured in situ during the FTO plasma reduction. The model of the reference FTO layer on glass is extended to describe time evolution of the metallic Sn reduction from FTO.

3.1. Optical model of the FTO layer on glass substrate

Figure 2 shows multi-layered model of the reference sample [called Sample (0)] of FTO layer on SLG schematically. The structure of the sample observed on cross-sectional TEM image in Fig. 1 is approximated by a model with five layers. The top layer [L(3)] representing the surface roughness is followed by the thick layer of FTO [L(2)]. In between FTO layer and SLG substrate the transition double-layer was observed by TEM in Fig. 1. This layer is often used as a barrier to prevent diffusion of sodium from the SLG to the FTO and the amorphous part of the double-layer is often based on SiO_2 [8]. In the model, the diffusion barrier is effectively approximated as a single layer [L(1)]. Finally, the thick SLG substrate [L(0)] is terminated by the layer of Sn-rich SLG [L(-1)] at the back-side of the substrate. This layer originates from the float glass fabrication technology.

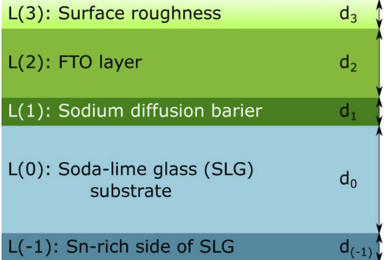

Fig. 2. Multi-layered model of the FTO on SLG Sample (0) derived from cross-section TEM images shown in Fig. 1. The thicknesses of particular layers from top to bottom are marked as d_3, d_2, d_1, d_0, and $d_{(-1)}$.

Figure 3 shows experimental data (symbols) measured on the reference FTO Sample (0) at the angles of incidence of 60°, 65°, and 70°, respectively. Oscillations in the spectral range from 1 eV to 4.5 eV originate from interferences (Fabry-Perot resonances) in the FTO layer. In this spectral range, optical absorption of the FTO is rather small and the measured optical response arrives from all sample materials. Towards lower energies, the oscillations are slightly attenuated due to the absorption of free electrons which are related to fluorine dopants. Above 4.5 eV the absorption of interband transitions is observed and the SE signal is sensitive primarily on the sample surface. Around the 2.5 eV, a phase-shift in the oscillations indicates the presence of an additional interface or layer. This layer had been identified as the sodium diffusion barrier [8]. The presence of the barrier was confirmed by TEM image shown in Fig. 1. Proposed multi-layered model is shown in Fig. 2 and the model optical functions of materials in particular layers are described as follows:

FTO layer L(2)

To describe complex optical function of the FTO layer L(2), namely contribution of the interband transition in UV region several models were tested, including simple Lorentz harmonic oscillator, Holden model [9], Tanguy model [10], and Tauc-Lorentz model [4]. Nevertheless, the

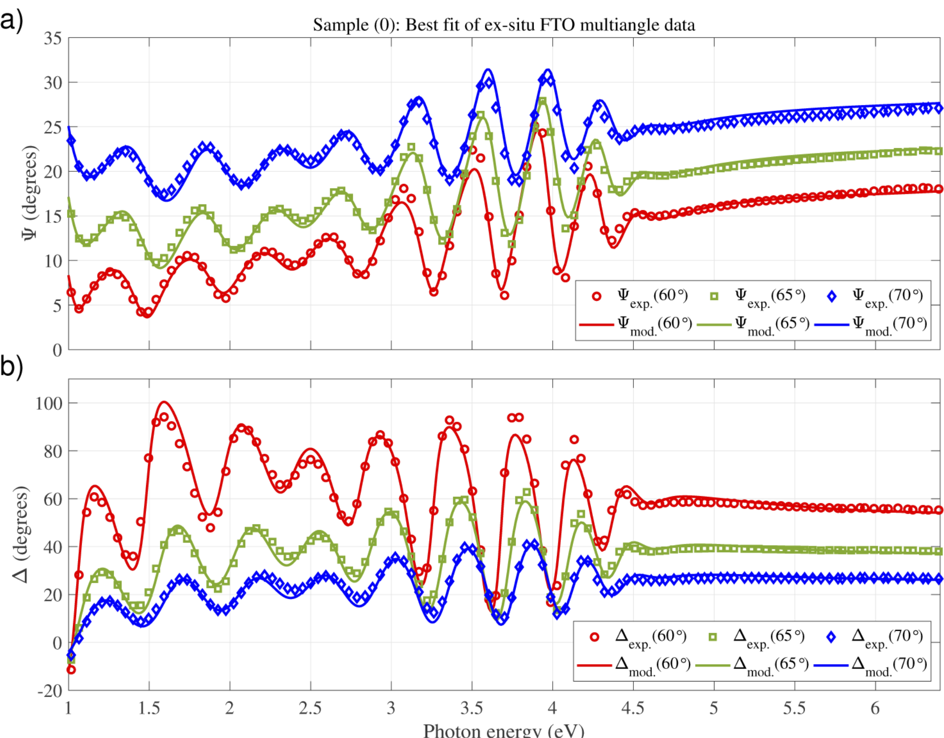

Fig. 3. Measured variable angle spectroscopic ellipsometric data of the reference FTO Sample (0) (symbols) are compared with modelled data (lines). Subplot a) shows the ellipsometric angle ψ and subplot b) shows the ellipsometric angle Δ measured at the angle of incidence of 60°, 65°, and 70°.

best match was obtained using model of $2DM_0$ critical point derived by Adachi [11]:

$$\epsilon_{CP}(E) = -B\chi_{CP}^{-2}\left(1 - \chi_{CP}^{2}\right), \quad \text{where}: \quad \chi_{CP} = \frac{\hbar E + i\Gamma}{E_0}, \tag{3}$$

where B, Γ, and E_0 are the amplitude, the damping factor and the central energy of the oscillator, respectively. Complete optical function $\epsilon_{L(2)}(E)$ of the FTO layer L(2) is defined as following sum:

$$\epsilon_{L(2)}(E) = \epsilon_{1\infty} - \frac{\hbar^2}{\epsilon_0 \rho_n \left(\tau_n E^2 + i\hbar E\right)} + \epsilon_{CP}(E), \tag{4}$$

where $\epsilon_{1\infty}$ is the permittivity in infinity. The second therm is the Drude free electron model describing effect of dopants in the IR part of the spectra. It is defined with ϵ_0, ρ_n, and τ_n parameters representing the vacuum dielectric constant, resistivity (Ω·cm), and scattering time (fs), respectively [12].

Diffusion barrier L(1)

The layer L(1), describing sodium diffusion barrier, is parameterized by the Sellmeier term $\epsilon_{SL}(E)$ [13]:

$$\epsilon_{L(1)}(E) = \epsilon_{SL}(E) = \frac{A_n}{E_n^2 - E^2}, \tag{5}$$

where A_n and E_0 are the amplitude and the resonance energy, respectively. The Sellmeier oscillator describes effectively optical dispersion of the layer in spectral range between 1 eV and

Optics EXPRESS

4.5 eV, where the FTO layer L(2) is transparent (see interferences in FTO layer in Fig. 3). The contrast of the refractive indices between layers L(2) and L(1) results in the phase shift observed around 2.5 eV.

Surface roughness L(3)

Surface of the polycrystalline FTO layer is usually very rough. One of the possible way how to describe optical response of such a surface, i.e. phase change of reflected polarized light, is to use surface layer with optical functions modeled by the Bruggeman effective medium approximation (B-EMA) consisting of FTO and void [14,15].

$$f\frac{\epsilon_a-\epsilon}{\epsilon_a-2\epsilon}+(1-f)\frac{\epsilon_b-\epsilon}{\epsilon_b-2\epsilon}=0, \tag{6}$$

where f is the volume fraction of the constituent material with optical response function ϵ_a in matrix of ϵ_b material, and the effective optical response of the composite material is obtained by solving for ϵ. B-EMA approximation can be used to describe random surfaces with gradually reducing optical density (see [4]). In our case, it was necessary to use B-EMA with graded profile due to a relatively high and irregular surface roughness. To keep the model simple, we have divided the surface roughness layer into three slices with the same thickness (1/3 of the total fitted thickness d_3) consisting of different void and FTO mixtures with different volume fractions (f_1, f_2, and f_3) of void in every slice. Three slices have been used as the simplest model to sufficiently describe optical response in the UV part of the spectral range. Further increase of slices or using a gradient layer did not improve the model significantly. Moreover, the advantage of the proposed model with three slices of surface roughness is that it can be used effectively to describe the reduction of tin on the FTO surface later on.

Soda-lime glass substrate L(0) and L(-1)

The dielectric function of SLG substrate L(0) is described as a sum of Sellmeier and Tauc-Lorentz oscillators with parameters directly adopted from Ref. [16]. The dielectric function of thin film representing the Sn-rich back side L(-1) of the SLG substrate is obtained using the model consisting of Sellmeier, Lorentz [13] and Gaussian [17] oscillators in accordance with the paper from Junda and Podraza [16]. However, the values of these parameters are adjusted to fit our reference Sample (0). Resulting parameters describing the substrate consisting of layers L(0) and L(-1) are summarized in Table 1. All these parameters are kept constant during further modeling.

Table 1. Parameters describing SLG substrate [layer L(0)] covered by Sn-rich SLG layer L(-1). In cases where no units are listed, the parameter is dimensionless or dimension is specified in the table as it can vary in different models.

Fit quality: χ^2 = 2.8		Optical Constants				
Layer	Description	Expression	A_n	E_n (eV)	Γ_n (eV)	E_{gn} (eV)
L(0)	SLG	$\epsilon_{1\infty}$ = 1				
bulk		Sellmeier	(1100 ± 200) (eV)^2	39.8 ± 0.5	-	-
		Tauc-Lorentz	(13 ± 4) eV	10.3 ± 0.7	0.07 ± 0.01	3.49 ± 0.02
L(-1)	Sn-rich SLG	Sellmeier	(492 ± 2) (eV)^2	14.83 ± 0.03	-	-
$d_{(-1)}$ = 63.1 ± 0.1 nm		Lorentz	0.022 ± 0.002	4.8 ± 0.5	14 ± 2	-
		Gaussian	0.346 ± 0.004	5.718 ± 0.002	0.752 ± 0.006	-

3.1.1. Fitting and results

Designed multi-layered optical model is fitted to measured data using the merit function χ^2 [Eq. (2)]. Data measured at the angles of incidence of 60°, 65°, and 70° is fitted simultaneously with the same fitting parameters, which are bound between models for each angle. The fitting

Optics EXPRESS

parameters were: the thicknesses d_1, d_2, and d_3 of the layers L(1), L(2), and L(3), respectively, volume fractions of B-EMA divided in three sublayers (f_1, f_2, f_3), and parameters of used dielectric functions. In the model, only two parameters were fixed: the thickness of the SLG substrate d_0 = 2.2 mm and the angle of incidence.

Figure 3 shows the best fit of multi-angle SE data measured ex-situ on the reference Sample (0) of FTO layer on SLG. There is a very good agreement between modeled and measured data for each angle of incidence which proves a good robustness of designed model.

Presented model is robust enough to describe samples of FTO layer on SLG substrates provided by different commercial suppliers and to reproduce ex-situ and in situ experimental data. Furthermore, this stable model is developed with a small number of fitting parameters describing geometry of the structure and defining optical functions of present layers. In addition, the model is stable and do not require fixing of fitting parameters. For comparison, measured spectra and fit of the sample from a different supplier can be found in Supplement 1 in Fig. S1 with the detailed parameters acquired from fit shown in Supplement 1, Table S1. Finally, a comparison of FTO optical functions for both substrates is plotted in Supplement 1, Fig. S2.

Results of fitting procedure are summarized in Fig. 4 and Table 2. Figure 4(a) shows TEM micrograph overlapped by thicknesses of layers achieved by the SE data fitting. Partial misalignment between fitted and observed thickness profile is probably caused by inhomogeneity of the FTO surface and by the preparation of the sample for TEM observation, i.e. polishing of the thin cross-sectional sample slice, where perpendicularity of the cut to the surface is not guaranteed. Figure 4(b) shows fitted dielectric function of FTO with fitted parameters of model dielectric functions, thicknesses, and merit function χ^2 summarized in Table 2.

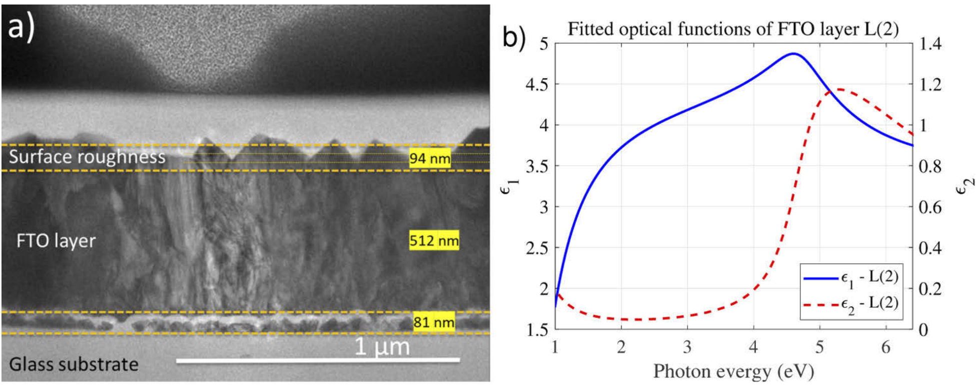

Fig. 4. a) TEM micrograph with overlapped fitted thicknesses of layers. Thicknesses are taken from best-fit in Table 2. b) Fitted optical functions of the FTO layer L(2).

3.2. Model and optical functions of reference Sn

To determine optical functions of metallic Sn, the reference sample of a 250 nm (nominal) thick Sn layer on Si wafer was prepared by the thermal evaporation. Since the thickness of the evaporated Sn layer is much higher than the light penetration depth (which is less than 35 nm for the whole measured spectral interval), the Si substrate has no influence on the measured SE data. Therefore, the Sn layer can be modeled as a semi-infinite bulk material. SE data measured on the Sn sample were fitted using the Kramers-Kronig consistent B-spline dielectric function model [18]. Figure 5 shows on the left subplot the best fit of the measured ellipsometric angles ψ and Δ. Experimental data were measured directly in the vacuum chamber of the reactor using the same ellipsometer as during in situ measurements. Native surface oxide of the Sn film was not removed from the sample. The data were measured at the angle of incidence of 72.1° (determined by

Table 2. All fitting parameters describing the part of Sample (0) consisting of diffusion barrier [layer L(1)], FTO layer L(2) and surface roughness layer L(3). In cases where no units are listed, the parameter is dimensionless.

Fit quality: χ^2 = 16	Optical Constants		
Layer	Description	Expression	Parameters
L(3)	FTO+void	B-EMA	f_1 = 0.179 ± 0.005 (void)
d_3 = 95 ± 2 nm			f_2 = 0.461 ± 0.008 (void)
			f_3 = 0.87 ± 0.01 (void)
L(2)	FTO		ϵ_{inf} = 3.67 ± 0.01
d_2 = 512.4 ± 0.7 nm		Drude	τ_n = (9.0 ± 0.3) fs
			ρ_n = (0.000216 ± 0.000006) Ω·cm
		2DM0	B = 1.44 ± 0.02
			E_0 = (4.67 ± 0.01) eV
			Γ = (0.350 ± 0.004) eV
L(1)	diffusion barrier	Sellmeier	A_n = (96.4 ± 0.2) $(eV)^2$
d_1 = 81.8 ± 0.3 nm			E_n = (5.974 ± 0.004) eV

system calibration). The right subplot shows resulting optical function of the Sn used for further studies.

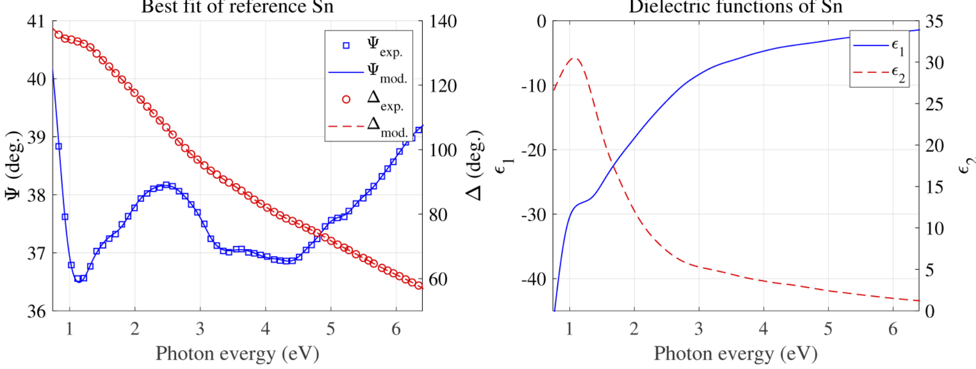

Fig. 5. Measured spectroscopic data of the reference Sn sample (symbols) are compared with model (lines). Left subplot shows the ellipsometric angle ψ (squares) and Δ (circles) measured at the angle of incidence of 72.1° (number of displayed experimental points was reduced for better visibility). Right subplot shows obtained real and imaginary part of Sn dielectric function ϵ_1 and ϵ_2, respectively.

3.3. In situ study of reduction processes of metallic tin from FTO

In this section, we study the process of Sn reduction from FTO. We have to develop a new optical model, which allows to incorporate increasing amount of Sn into the default model of FTO sample, which will enable us to study the effect of treatment duration on the Sn reduction process. Because of the substantial FTO surface roughness, the model cannot be realized by simply adding a single Sn layer as it would be the case for flat substrates. We have studied three different substrates exposed to the hydrogen plasma for 120, 180 and 240 s for Sample (1), Sample (2), and Sample (3), respectively. Our approach is separated into two steps applied to the data measured in situ.

At the beginning of study of each reduction process, when a new sample with FTO layer was loaded into the reactor. The parameters are fitted following the model described in Section 3.1. This adjustment is essential step for in situ analysis, because it can compensate for observed variations between studied substrates from different batches or providers.

In the next step, the effective medium surface roughness layer L(3) is changed from the two-component FTO/void B-EMA mixture to the three-component FTO/void/Sn B-EMA mixture, which enables to model the emerging metallic Sn on the sample surface during the hydrogen plasma treatment. In the three-component B-EMA, the ratios between values of FTO/void volume fractions f_1, f_2, and f_3 (see Table 2) were conserved from the first step before the plasma has been applied. A new B-EMA layer (L3) is defined between the gradient layer and Sn material introduced with the volume fraction f_{Sn}. The optical functions of Sn are taken from the reference sample studied in Section 3.2.

The model is used for the in situ monitoring of the reduction process, while only Sn-volume fraction f_{Sn} and the thickness d_3 of the surface roughness layer L(3) are the fitted parameters. The amount of Sn in nanoparticles per square unit then corresponds to the amount of material, which would cover the same area in an effective continuous Sn layer of thickness d_{Sn} as illustrated in the Fig. 6. The thickness of this Sn layer is obtained as a product of the thickness of surface roughness layer d_3 and the Sn volume fraction f_{Sn}:

$$d_{Sn} = f_{\mathrm{Sn}} \cdot d_3. \tag{7}$$

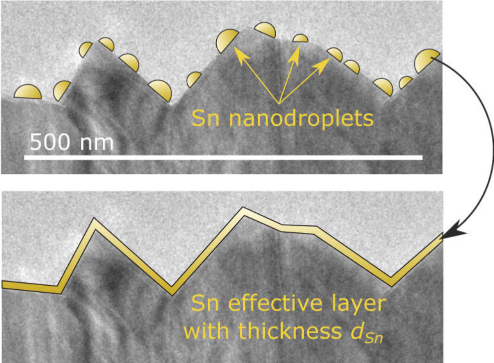

Fig. 6. Schematic drawing of Sn nanodroplets on the sample surface which can be represented by the effective Sn layer of thickness d_{Sn}.

Figure 7 shows measured and fitted SE data (Ψ and Δ) of Sample (3) before reduction and at the end of the plasma reduction process (blue and green lines, respectively). Both subplots (a) and (b) show clear change in the optical response of the studied sample after 240 s of the plasma reduction process. For data before the reduction process (blue curves) fitted parameters of the model were as follows: $f_{\mathrm{Sn}} = (0.1 \pm 0.1)$ %, $d_3 = 76.1 \pm 1.2$ nm. The correlation coefficient between these parameters is 0.6. After the reduction for 240 s, the fit results are $f_{\mathrm{Sn}} = (4.3 \pm 0.1)$ %, $d_3 = 81.4 \pm 1.1$ nm, the effective Sn thickness $d_{Sn} = 3.5$ nm, and the correlation coefficient is 0.2. Despite the model not being perfect, the effect of the Sn in the three-component B-EMA in the layer L(3) describes the change of the measured response well with only two fitting parameters and with low correlation coefficient. This makes the proposed model very robust and sufficiently simple for the real-time in situ data analysis.

The developed model was used for real-time monitoring of three FTO samples, while plasma exposure time was 120, 180, and 240 s. The SE data were measured every 10 s during the process to closely monitor the time evolution of tin increase. Figure 8 shows the effective thicknesses of

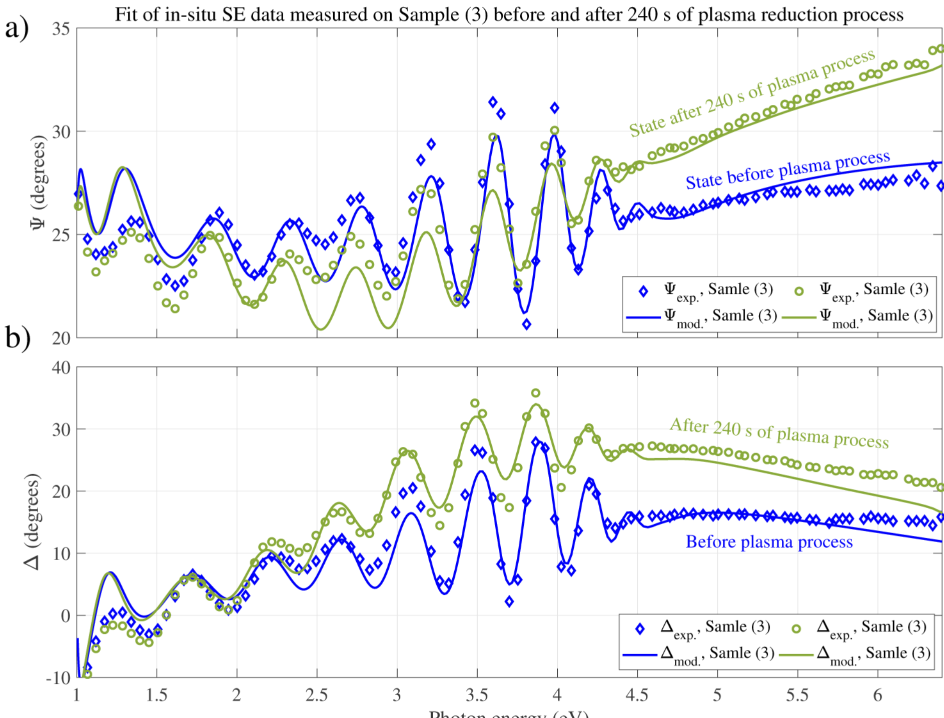

Fig. 7. Spectroscopic ellipsometric in situ data measured and modeled for the Sample (3) in the reactor chamber before reduction process (blue symbols and lines, respectively) and at the end of the process after 240 s reduction (green symbols and lines, respectively). Subplot a) shows the ellipsometric angle ψ and subplot b) shows the ellipsometric angle Δ measured at the angle of incidence of 72.1° for the in situ measurements.

Sn reduced from FTO by hydrogen plasma as a function of plasma exposure time fitted every 10 s. The initial point, time $t = 0$ s, is the point of the hydrogen plasma ignition. The effective Sn film thickness is calculated from Eq. (7) using the fitted parameters. The amount of Sn increases monotonously with the exposure time until the plasma is switched off, which is marked with a color arrow for each sample. After finishing the plasma process, the effective Sn film thickness is constant in time, which is related to the termination of the reduction process and surface of the sample being stable.

In situ observations of the amount of Sn reduced from FTO is critical for the control of the catalyst density, which has a direct impact on the density of SiNWs grown using vapor-liquid-solid (VLS) process. It has been shown that the SiNW density has a direct impact on the performance of the solar cells fabricated on the top of them [19]. The robustness of the developed model enables us to fit different samples of FTO on SLG substrates from different batch and/or different manufacturer. This is the key property of the model which enables its application when samples or devices are being prepared from FTO on SLG substrates. In particular, it enables to develop models for in situ monitoring of the sample during different stages of the grow process which is important for controllable and repeatable device fabrication.

3.3.1. Comparison of SE and SEM

The Sample (1), Sample (2), and Sample (3) were also studied by scanning electron microscopy (SEM, HITACHI S-4800) after previously described hydrogen plasma reduction processes.

Optics EXPRESS

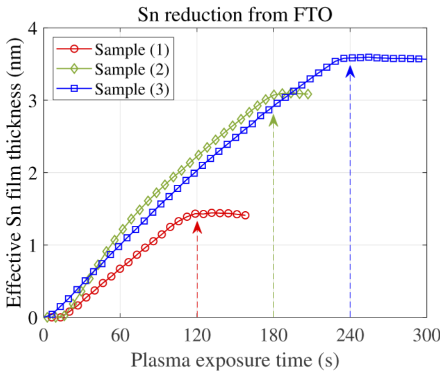

Fig. 8. Effective Sn film thickness as a function of plasma exposure time. Samples exposed to plasma treatment for 120 s (red), 180 s (green) and 240 s (blue) are compared.

Figure 9 shows micrographs of the FTO surface before reduction and after 120, 180, and 240 s of the reduction process. To compare amount of the reduced Sn, the Sn nanoparticles were measured and counted with each diameter from a micrometer square area noted. Volume of the reduced Sn was estimated assuming a half-sphere approximation of the shape of the reduced Sn nanoparticles. The effective thickness of the reduced Sn was estimated by dividing the acquired volume by the size of the observed area. The area of rough surfaces was angle-corrected using TEM observations from Fig. 1. Bottom subplot in Fig. 9 compares the effective thicknesses of the Sn layer estimated from fitting of SE data and from the SEM micrographs. The subplot shows better agreement for longer reduction time and worse for the short reduction time. The differences between results from SE and SEM are caused mainly by intrinsic inaccuracies in assumed nanoparticle shapes, surface area estimation and some imperfections in optical model.

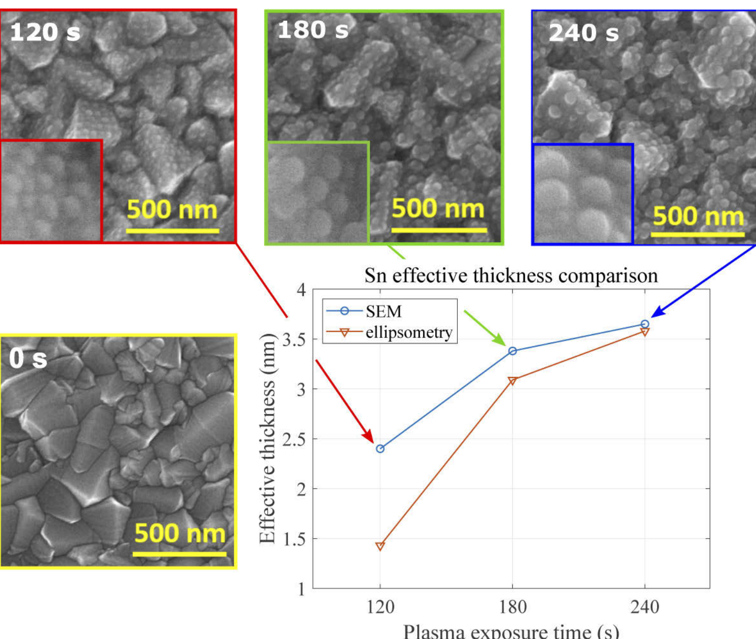

Fig. 9. Effective Sn film thickness from various plasma exposure times. Samples exposed to plasma treatment for 120 s (red), 180 s (green) and 240 s (blue) are compared.

Observations of nanoparticles in Fig. 9 show that after shorter reduction time, the shapes are far from half spheres, more closer to spherical caps. If we assume the same Sn nanoparticle sizes and spacial distributions as determined from SEM analysis, but a variation in shapes, the effective Sn thicknesses established from spectroscopic ellipsometry correspond to the nanoparticle shapes of sphere caps with heights of 0.30, 0.46, and 0.48 multiple of sphere diameters for reduction times of 120, 180, and 240 s, respectively. With longer reduction time, nanoparticles become closer to half-spheres. For 240 s of the reduction process, effective thickness of the reduced Sn calculated for half-spheres matches almost perfectly the effective thickness estimated from SE data analysis.

4. Conclusions

We have developed the layered model of the FTO films with barrier against the sodium diffusion prepared on soda-lime glass substrate. The model was constructed in agreement with the TEM micrographs. The robustness of the optical model was tested by fitting data, taken by spectroscopic ellipsometry at multiple incident angle, simultaneously. The parameterization of the model is sufficiently general to be used with optical SE data measured in different experimental systems on various commercial substrates available on a market.

We have also included Sn optical function into the developed model of the rough FTO film in order to be able to describe the FTO reduction process. The layered model of the FTO on glass substrate was extended by the three-component FTO/void/Sn B-EMA surface layer and used to successfully analyze the reduction processes using the hydrogen plasma. After the reduction, samples were studied by the SEM micrographs and the amount of reduced Sn calculated from the optical model developed for in situ SE is in a good agreement with values obtained from SEM.

The developed optical model allows the SE monitoring of Sn reduction to be used as fast, non-destructive, real-time procedure compatible with the industrial technology, such as PECVD. Combination of in situ SE with the presented model represents a very convenient and cost effective way to control the Sn reduction process. This enables optimization and better quality control of processes used to fabricate nanowire devices grown on FTO substrates.

Funding. Dům zahraniční spolupráce (EMP-CZ-MOP-2-013, MP-CZ-MOP-2-013); Horizon 2020 Framework Programme (FET-Open Grant No. 863155, s-NEBULA); Horizon 2020 Framework Programme (19ENG05 NanoWires); Agence Nationale de la Recherche (ANR-10-EQPX-50, ANR-15-CE05-0019); Ministerstvo Průmyslu a Obchodu (FV20020); Ministerstvo Školství, Mládeže a Tělovýchovy (16013/0001791, SP2020/71).

Acknowledgments. The authors would like to acknowledge the Centre Interdisciplinaire de Microscopie électronique de l'X (CIMEX). Partial support from the Horizon 2020 Framework Programme of the European Commission under FET-Open Grant No. 863155 (s-Nebula), IT4Innovations National Supercomputing Center – Path to Exascale (Project No. CZ02.1.01/0.0/0.0/16013/0001791), French state managed by the National Research Agency under the Investments for the Future program under the references ANR-10-EQPX-50 pole NanoTEM, the French Agence Nationale de la Recherche under the contract numbers INDEED ANR-15-CE05-0019, EEA grant (Project No. EMP-CZ-MOP-2-013), FV20020, and student grant system (Project No. SP2020/71) is acknowledged. We would like to acknowledge funding by the project 19ENG05 NanoWires which has received funding from the EMPIR programme co-financed by the Participating States and from the European Union's Horizon 2020 research and innovation programme.

Disclosures. The authors declare no conflicts of interest.

Data availability. Data underlying the results presented in this paper are not publicly available at this time but may be obtained from the authors upon reasonable request.

Supplemental document. See Supplement 1 for supporting content.

References

1. S. Misra, L. Yu, M. Foldyna, and P. Roca i Cabarrocas, "New approaches to improve the performance of thin-film radial junction solar cells built over silicon nanowire arrays," IEEE J. Photovoltaics **5**(1), 40–45 (2015).
2. M. Al-Ghzaiwat, A. Foti, A. Nuesslein, L. Halagacka, J. Meot, A. Labouret, R. Ossikovski, P. Roca i Cabarrocas, and M. Foldyna, "Toward efficient radial junction silicon nanowire-based solar mini-modules," Phys. Status Solidi (RRL)–Rapid Res. Lett. **13**(2), 1800402 (2019).

3. Z. Mrázková, M. Foldyna, S. Misra, M. Al-Ghzaiwat, K. Postava, J. Pištora, and P. Roca i Cabarrocas, "In-situ mueller matrix ellipsometry of silicon nanowires grown by plasma-enhanced vapor-liquid-solid method for radial junction solar cells," Appl. Surf. Sci. **421**, 667–673 (2017).
4. M. Akagawa and H. Fujiwara, "High-precision characterization of textured a-Si:H/SnO_2:f structures by spectroscopic ellipsometry," J. Appl. Phys. **110**(7), 073518 (2011).
5. I. Ngo, B. O'Donnell, J. Alvarez, M. Gueunier-Farret, J.-P. Kleider, L. Yu, and P. Roca i Cabarrocas, "Catalyst formation and growth of sn-and in-catalyzed silicon nanowires," MRS Online Proc. Libr. Arch. **1258**, 1258-P04-51 (2010).
6. H. Fujiwara, *Spectroscopic ellipsometry: principles and applications* (John Wiley & Sons, 2007).
7. D. Marquardt, "An algorithm for least-squares estimation of nonlinear parameters," J. Soc. Ind. Appl. Math. **11**(2), 431–441 (1963).
8. Y. Yan, X. Li, R. Dhere, M. Al-Jassim, K. Jones, M. Young, and M. Scott, "SiO_2 as barrier layer for na out-diffusion from soda-lime glass," in *2010 35th IEEE Photovoltaic Specialists Conference*, (2010), pp. 002519–002521.
9. T. Holden, P. Ram, F. H. Pollak, J. Freeouf, B. Yang, and M. Tamargo, "Spectral ellipsometry investigation of $Zn_0.53Cd_0.47$Se lattice matched to InP," Phys. Rev. B **56**(7), 4037–4046 (1997).
10. C. Tanguy, "Analytical expression of the complex dielectric function for the hulthen potential," Phys. Rev. B **60**(15), 10660–10663 (1999).
11. S. Adachi, "Model dielectric constants of GaP, GaAs, GaSb, InP, InAs, and InSb," Phys. Rev. B **35**(14), 7454–7463 (1987).
12. T. E. Tiwald, D. W. Thompson, J. A. Woollam, W. Paulson, and R. Hance, "Application of IR variable angle spectroscopic ellipsometry to the determination of free carrier concentration depth profiles," Thin Solid Films **313-314**, 661–666 (1998).
13. H. Tompkins and E. A. Irene, *Handbook of ellipsometry* (William Andrew, 2005).
14. D. Aspnes, J. Theeten, and F. Hottier, "Investigation of effective-medium models of microscopic surface roughness by spectroscopic ellipsometry," Phys. Rev. B **20**(8), 3292–3302 (1979).
15. H. Fujiwara, J. Koh, P. Rovira, and R. Collins, "Assessment of effective-medium theories in the analysis of nucleation and microscopic surface roughness evolution for semiconductor thin films," Phys. Rev. B **61**(16), 10832–10844 (2000).
16. M. M. Junda and N. J. Podraza, "Optical properties of soda lime float glass from 3 mm to 148 nm (0.41 meV to 8.38 eV) by spectroscopic ellipsometry," Surf. Sci. Spectra **25**(1), 016001 (2018).
17. K.-E. Peiponen and E. Vartiainen, "Kramers-kronig relations in optical data inversion," Phys. Rev. B **44**(15), 8301–8303 (1991).
18. B. Johs and J. S. Hale, "Dielectric function representation by B-splines," phys. stat. sol. (a) **205**(4), 715–719 (2008).
19. S. Misra, L. Yu, M. Foldyna, and P. Roca i Cabarrocas, "High efficiency and stable hydrogenated amorphous silicon radial junction solar cells built on vls-grown silicon nanowires," Sol. Energy Mater. Sol. Cells **118**, 90–95 (2013).

158.196.184.115 {ts '2021-11-19 04:35:07'}